2013 IEEE/RSJ International Conference on
Intelligent Robots and Systems (IROS)
November 3-7, 2013. Tokyo, Japan

Geometry-Aided Angular Acceleration Sensing of Rigid Multi-Body Manipulator Using MEMS Rate Gyros and Linear Accelerometers

Juho Vihonen[1], Janne Honkakorpi[2], Jouni Mattila[2], and Ari Visa[1], *Senior Member, IEEE*

Abstract— **We consider full motion state sensing of a rigid open-chain multi-body linkage assembly using rate gyros and linear accelerometers. The research is built upon micro-electro-mechanical systems (MEMS) components for low-cost "strap-down" implementation. Our emphasis is on direct lag-free joint angular acceleration sensing, for which a novel multi-MEMS configuration is motivated by motion control requirements. By using the multi-MEMS configuration, the bandwidth of the angular acceleration sensed is mostly proportional to the physical distances of linear accelerometers. The related joint position sensing, which is robust against linear and angular motion, is founded on the complementary and Kalman filtering principles for exclusive low delay. Experiments on a robotic vertically mounted three-link planar arm demonstrate the advantage of our key theoretical finding.**

I. INTRODUCTION

The main problem connected with magnetic or optical rotary encoders, two of the most popular single degree of freedom (DOF) joint angular sensors, is the limited bandwidth of derivatives of angular motion. If differentiated from the encoder position readings indirectly as usual, a considerable density of high-frequency perturbations is superimposed on the reconstructed angular velocity and, particularly, on the angular acceleration readings, see e.g. [1]. The required perturbation attenuation comes at the cost of lag, see e.g. [2], which impairs the transient response of control strategy. As a significant advantage over the contact-type joint angular sensors, the miniaturized micro-electromechanical systems (MEMS) sensors, such as linear accelerometers, rate gyros, and magnetometers, may be simply "strapped down" to a body requiring no contact to a rotation axle. We consider gyro-aided high-bandwidth joint position sensing endowed with direct algebraic calculation of the angular acceleration components. In view of our previous work [3], where simple indirect rate gyro differentiation was considered, a significant leap forward is presented.

Since optional sensors, such as magnetometers, are unusable in many practical situations [4], there is a pressing motivation for producing high-bandwidth manipulator motion state estimates based solely on MEMS rate gyro and accelerometer readings. Previously, motion sensing based on MEMS has been under consideration for use in multi-DOF robots [5], cranes and excavators [6], and biomedical setups [7] often founded upon simplified hinge joint models [8]. To circumvent the difficulties related to the indirect motion derivatives using contact-type angular sensors, we consider a minimum MEMS configuration of triaxial linear accelerometers and rate gyros and a novel multi-MEMS configuration with added three linear accelerometers for direct algebraic angular acceleration sensing. Our multi-MEMS configuration, inspired by [9], is stable, practically lag-free, and not subject to error accumulation, in spite of the inherent MEMS scale factor errors in relatively fast motion. Noteworthy, the bandwidth of our algebraic angular acceleration sensing depends mostly on the mutual distance between the linear accelerometers.

This paper is organized as follows. Sect. II provides an overview of the MEMS models, our geometrical manipulator model, as well as the MEMS configurations, the theoretical basis of this work. As a whole, the MEMS motion sensing is ideally suited for real-time implementation on embedded hardware platforms, which we demonstrate in Sect. III by a three-link planar arm rig. Although our MEMS components, a set of six combined single-axis ± 100 deg/s rate gyros and triaxial linear $\pm 2g$ accelerometers [10], allow 2-DOF joint position sensing based on the force of gravity, the planar vertical case is of theoretical and practical interest. Without loss of generality the MEMS error propagation is founded on exactly the same principles in a fully three-dimensional case. Thus, for analytical simplicity, we will briefly study a standard algebraic single-axis inclination estimate, which is listed by many MEMS accelerometer manufacturers, and refine it by a complementary filter, which represents the theoretical basis for many gyro-aided feedback designs, see e.g. [11], [12], [13]. Our experimental comparison is founded on optimal truncated finite difference calculation of the motion derivatives, see [14]. Finally, the conclusions are drawn in Sect. IV.

II. OBSERVATION MODEL AND ESTIMATION

In this section, we provide observation models for strap-down MEMS accelerometers and rate gyros by studying a geometrical open-chain kinematics estimation problem. In consequence, accurate link inclination sensing in accelerative motion is possible only without notable simplifications or decoupling of the related kinematic quantities.

A. Geometrical rigid body model

Consider an assembly of two or more rigid links connected by means of joints. Three-dimensional frames of rectangular (xyz) axes are attached to the center of each joint and the

This work was supported by the Academy of Finland under the project "Sensor Network Based Intelligent Condition Monitoring of Mobile Machinery", grant no. 133273.

[1]J. Vihonen and A. Visa are with the Department of Signal Processing, Tampere University of Technology, FI-33101, Finland.

[2]J. Honkakorpi and J. Mattila are with the Department of Intelligent Hydraulics and Automation, Tampere University of Technology, FI-33101, Finland. E-mail: firstname.surname@tut.fi

978-1-4673-6357-0/13/$31.00 ©2013 IEEE

links are directed along their y-axes. Let R_i denote the $3{\times}3$ body fixed rotation matrix, $\det(R_i) = 1$ and $R_i^T = R_i^{-1}$, relating the i^{th} link frame to the inertial reference frame (XYZ) as usual. The assembly is illustrated in Fig. 1, where length of the i^{th} (bar-like) link is denoted by l_i. The "ground" frame R_0 is fixed to a (stationary) base platform. Subsequently, we will neglect the Earth's angular rate (15 deg/h) because of the low MEMS sensitivity and large noise density.

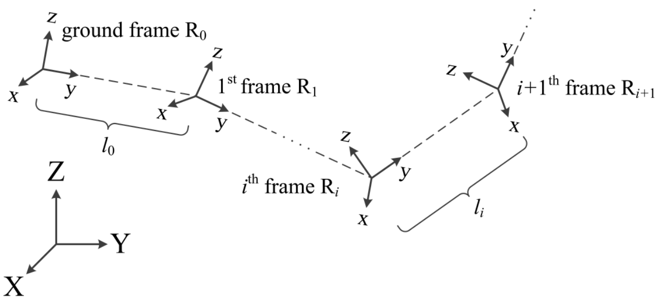

Fig. 1. Rigid body model. Links are connected by rotary joints.

The angular velocity, as seen by a MEMS component rate gyro attached to the i^{th} link, $i = 1, 2, \ldots$, can be expressed in the i^{th} joint's frame by

$$\tilde{\Omega}_i = (I + S_i)\Omega_i + b_i + \mu \in \mathbb{R}^{3\times 1}, \tag{1}$$

where I is the identity matrix, Ω_i is the total true rate value, S_i is the scale factor error expressed as a percentage of Ω_i, b_i denotes a constant or slowly time-varying gyro bias, and μ denotes additive measurement noise. Because most triaxial MEMS rate gyros are assembled as three single-axis gyros, we may assume low cross-axis coupling factors; i.e., S_i is a diagonal matrix. In view of the rigid body assumption, one may write

$$\Omega_i = \omega_i + \sum_{m=0}^{i-1} R_i^T R_m \omega_m \tag{2}$$

denoting that the total true rate is the sum of the angular velocities produced by the i^{th} joint, given by ω_i, and each of the preceding joints expressed in frame i.

The linear accelerations, as seen by a MEMS component accelerometer attached to the i^{th} link, $i = 1, 2, \ldots$, can be expressed by

$$a_i = (I + S_i)(v_i - R_i^T g) + b_a + \mu_a \in \mathbb{R}^{3\times 1}, \tag{3}$$

where S_i is the scale factor error, g is the gravitational field $g = |g_0| e_3$, $|g_0| \approx 9.8$ m/s^2, b_a is a bias term, and μ_a denotes additive measurement noise. Because most triaxial MEMS accelerometers are assembled as three single-axis accelerometers, we may again assume low cross-axis coupling factors in S_i. If $\times$ denotes the cross product, the instantaneous linear acceleration v_i can be given as

$$\begin{aligned} v_i \;=\;& \alpha_i \times d_i + \omega_i \times (\omega_i \times d_i) + \\ & \sum_{n=0}^{i-1} \Big((R_i^T R_n \alpha_n) \times d_n + \\ & \quad (R_i^T R_n \omega_n) \times \big((R_i^T R_n \omega_n) \times d_n \big) \Big), \end{aligned} \tag{4}$$

where α_i is the true angular acceleration produced by the i^{th} joint, the vectorial distance from the i^{th} joint's rotation center is

$$d_i = [0 \;\; p_i^y \;\; p_i^z]^T = p_i \tag{5}$$

and for the other rotation centers

$$d_n = R_i^T \sum_{m=n}^{i-1} R_m [0 \;\; l_m \;\; 0]^T + d_i \tag{6}$$

for a low number of coordinate system transforms. The position (5) is typically known to a high degree of accuracy. Given that the "ground" frame is stationary, we assume $l_0 = 0$, $R_0 = I$, and $\omega_0 = \alpha_0 = d_0 = [0 \;\; 0 \;\; 0]^T$ for clarity. We will also take the Z-axis rotation of R_i for granted, since it is not observable from the accelerometer readings.

To construct a 2-DOF estimate of the "true" rotation R_i from the accelerometer readings (3), complete definition of (4) is required. For a high-bandwidth low-delay estimate, identification of gyro bias in (1) is also needed. As a step toward the perfection of both at once, we will apply the postulated assembly model in a suboptimal manner, since the signals (1) and (3) may not be modeled as random processes with fully known spectral characteristics.

B. Minimum and novel multi-MEMS configuration

Consider the problem of quantifying the relative rotational motion of each joint in the discussed assembly. With MEMS component accelerometers and rate gyros, none of the motion states of the i^{th} joint, the position, angular velocity or angular acceleration, can be measured directly for $i = 1, 2, \ldots$ in the general case. Next, we will base the angular velocity and acceleration computation on simple kinematic principles.

An estimate of the angular velocity of the i^{th} joint, as sensed by a MEMS component rate gyro attached to the i^{th} link, $i = 1, 2, \ldots$, can be given by applying (2) as

$$\hat{\omega}_i = \tilde{\Omega}_i + \hat{b}_i - \sum_{m=0}^{i-1} R_i^T R_m \hat{\omega}_m \tag{7}$$

where we have introduced $\hat{b}_i$ to cancel the bias in (1). The differentiation

$$\hat{\alpha}_i = \dot{\hat{\omega}}_i \tag{8}$$

yields an estimate of the angular acceleration of the i^{th} joint. Alternatively, if a triaxial plus additional three linear accelerometers are attached and the all six are organized into three pairs, we may write a direct estimate of the angular acceleration of the i^{th} joint as follows:

$$\hat{\alpha}_i = \begin{bmatrix} (a_i^{z_1} - a_i^z - \delta_1^z)/d_i^{y_1} - \hat{\omega}_i^y \hat{\omega}_i^z \\ -(a_i^{z_2} - a_i^z - \delta_2^z)/d_i^{x_2} + \hat{\omega}_i^x \hat{\omega}_i^z \\ (a_i^{y_2} - a_i^y - \delta_2^y)/d_i^{x_2} - \hat{\omega}_i^x \hat{\omega}_i^y \end{bmatrix} \tag{9}$$

where, according to (4), we must calculate

$$\begin{aligned} \delta_j \;=\;& \sum_{n=0}^{i-1} \Big((R_i^T R_n \hat{\alpha}_n) \times (p_i^j - p_i) + \\ & (R_i^T R_n \hat{\omega}_n) \times \big((R_i^T R_n \hat{\omega}_n) \times (p_i^j - p_i) \big) \Big) \end{aligned} \tag{10}$$

for a configuration of the additional accelerometers positioned at

$$p_i^1 = p_i + \begin{bmatrix} 0 \\ d_i^{y_1} \\ 0 \end{bmatrix}, p_i^2 = p_i + \begin{bmatrix} d_i^{x_2} \\ 0 \\ 0 \end{bmatrix} \tag{11}$$

so that $d_i^{y_1} > 0$ and $d_i^{x_2} \neq 0$. Note that the angular acceleration components in (9) require prior knowledge of the angular velocities about the xyz-axes, but only the added three linear acceleration components co-directional with the y and z axes of the accelerometer (3) positioned at p_i are needed.

The triaxial accelerometer and rate gyro configuration related to the estimates (7) and (8) is shown in Fig. 2 for $p_i^z = 0$. This set of MEMS components represents a minimum configuration in view of Sect. II-A. Our multi-MEMS

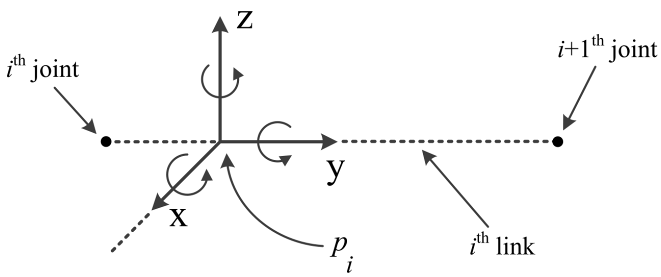

Fig. 2. A minimum configuration of three linear accelerometers attached to the i^{th} link. Angular velocities about the shown sensitive axes are measured by a triaxial rate gyro.

configuration related to the estimates (7) and (9) is shown in Fig. 3. The added single-axis and biaxial accelerometers eliminate contributions of the gravitational field in (9).

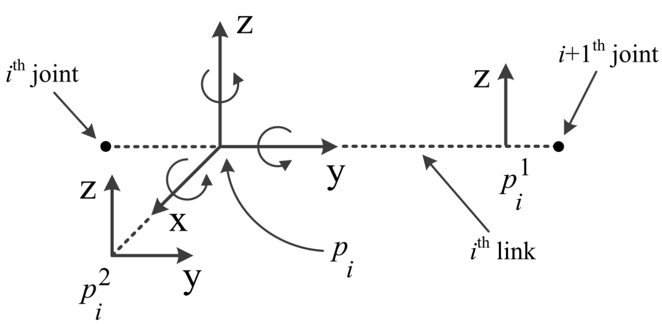

Fig. 3. A configuration of six linear accelerometers and a triaxial rate gyro attached to the i^{th} link. If compared with Fig. 2, the added accelerometers with sensitive axes shown are used for direct angular acceleration sensing.

Note that we may write

$$\hat{\alpha}_i = \alpha_i + b_\alpha + \mu_\alpha \tag{12}$$

where b_α is a low-frequency bias term and μ_α denotes higher frequency perturbations cumulated from different sensors. If we assume a low-noise bias-identified triad of high-bandwidth rate gyros when computing (9) in circular motion and omit all the scale factor errors embedded in (12), we obtain the "true" i^{th} joint angular acceleration by

$$\lim_{||p_i^1||,||p_i^2|| \to \infty} \hat{\alpha}_i = \alpha_i. \tag{13}$$

The finding is significant as it states that, by using the latest MEMS components, the perturbation contributions are mostly proportional to the physical distances of the z-axis and yz-axial accelerometers at p_i^1 and p_i^2 with respect to the triaxial accelerometer at p_i. The asymptotic limit is thereby achievable, though the sensing ranges, sensor misalignment, and linearity affect the direct sensing (9) in practice.

C. Instantaneous acceleration compensation

Next, we will complete the geometrical analysis by showing that 2-DOF inclination sensing is feasible in real-time for the above MEMS configurations.

By replacing the "true" angular acceleration and angular velocity in (4) using (7) and either (8) or (9), an algebraic estimate of the instantaneous linear acceleration $\hat{v}_i$ can be written as

$$\hat{v}_i = v_i + b_v + \mu_v \tag{14}$$

where b_v is a bias term and μ_v denotes additive noise that is cumulated from different sensors, each with its own error characteristics. For an accelerometer (3) located at p_i, the above yields

$$a_i - \hat{v}_i \approx -R_i^T g \tag{15}$$

for which the required estimates of angular velocity (7) and acceleration given either by (8) or (9) can be obtained without complicated transforms as discussed in Sect. II-B.

The result (15) states that, when (14) is computed joint by joint from the 1st link to the i^{th}, we may construct a 2-DOF estimate of the "true" rotation R_i from the gravitational field even when the joints of the assembly are in accelerative motion. This applies for small angle rotations occurring between successive real-time updates of the link-wise inclinations. A high-enough sampling rate is thereby required.

III. Experiments

A mechanically simple vertically mounted three-link planar arm is constructed for motion sensing experiments, since it behaves like an ideal rigid multi-body assembly. In spite of the fact that (15) relates directly to the 2-DOF inclination of a rigid body, we will apply a widely-used 1-DOF algebraic inclination estimate and refine it by a straightforward gyro-aided fusion for both theoretical and analytical simplicity.

A. Single axis inclination sensing from gravity vertical

Suppose that the motion of a linkage assembly takes place in a vertical plane, joints are 1-DOF rotary and have their x-axes co-directional. Then, in view of link inclination sensing, an accelerometer's y-axis output follows the sine function and its z-axis follows the cosine function

$$\begin{aligned} a_i^y &\approx g_0 \sin(\theta_i) \\ a_i^z &\approx g_0 \cos(\theta_i) \end{aligned} \tag{16}$$

when the accelerometer is stationary. Algebraic inclination through a 360 deg range relative to gravity vertical can then be calculated by applying

$$\hat{\theta}_i = \arctan(a_i^y, a_i^z) \tag{17}$$

where $\arctan(\cdot)$ is the four quadrant inverse tangent function. However, the estimate is valid only for the special case where the gravity field alone acts on the accelerometer. To enforce the relationship (16) in accelerative motion, we calculate

$$\hat{\theta}_i = \arctan(a_i^y - \hat{v}_i^y, a_i^z - \hat{v}_i^z), \tag{18}$$

which is a direct generalization of (17).

For a high-bandwidth inclination estimate, any standalone integration of angular velocity readings without high-pass filtering of the gyro bias (1) will be susceptible to drift. Additionally, since (3) contains mostly high frequency perturbations, any accelerometer-based inclination estimate should be low-pass filtered. The following differential equation

$$\begin{bmatrix} \dot{\hat{\theta}} \\ \dot{\hat{b}} \end{bmatrix} = \begin{bmatrix} 0 & 1 \\ 0 & 0 \end{bmatrix} \begin{bmatrix} \hat{\theta} \\ \hat{b} \end{bmatrix} + \begin{bmatrix} k_{\mathrm{P}} \\ k_{\mathrm{I}} \end{bmatrix} (x_2 - \hat{\theta}) + \begin{bmatrix} 1 \\ 0 \end{bmatrix} x_1 \tag{19}$$

implements the required complementary low- and high-pass filters at the same time, where k_{P} is the proportional gain and k_{I} is the integral gain. Therefore, our discretized complementary filter can be given by

$$\begin{aligned} \begin{bmatrix} \hat{\theta}_i(t) \\ \hat{b}_i^x(t) \end{bmatrix} = \begin{bmatrix} 1 & T_{\mathrm{s}} \\ 0 & 1 \end{bmatrix} \begin{bmatrix} \hat{\theta}_i(t-1) \\ \hat{b}_i^x(t-1) \end{bmatrix} + \\ \begin{bmatrix} T_{\mathrm{s}} & 0.5T_{\mathrm{s}}^2 \\ 0 & T_{\mathrm{s}} \end{bmatrix} \begin{bmatrix} k_{\mathrm{P}} \\ k_{\mathrm{I}} \end{bmatrix} \big(x_2 - \hat{\theta}_i(t-1)\big) + \\ \begin{bmatrix} T_{\mathrm{s}} \\ 0 \end{bmatrix} x_1 \end{aligned} \tag{20}$$

where t denotes time, T_{s} is the sampling time, and $\hat{b}_i^x$ is the identified x-axis gyro bias. The first input can be given as

$$x_1 = \tilde{\Omega}_i^x \tag{21}$$

where x-directional rate of (1) is used, $i = 1, 2, \ldots$. The second input is

$$x_2 = \arctan(a_i^y - \hat{v}_i^y, a_i^z - \hat{v}_i^z) \tag{22}$$

as given by (18). Noteworthy, the assumption that the inputs of (19) are corrupted by stationary white noise produces a stationary Kalman filter (see e.g. [15]) that is identical in form to the complementary filter for $k_{\mathrm{I}} = 0$. However, to identify the gyros' bias values in real-time, we will choose $k_{\mathrm{P}} = 0.2$ and $k_{\mathrm{I}} = 0.02$ for the P- and I-type gains. This means that (20) implements a PI-type complementary filter, where the motion compensated inclination (18) from the accelerometer is used only as a long-term reference.

Since the motion permitted by our experimental setup is planar, the rotation matrices R_i can be efficiently updated for link-wise motion by writing

$$R_i \approx \hat{R}_i(\hat{\theta}_i) = \begin{bmatrix} 1 & 0 & 0 \\ 0 & \cos(\hat{\theta}_i) & -\sin(\hat{\theta}_i) \\ 0 & \sin(\hat{\theta}_i) & \cos(\hat{\theta}_i) \end{bmatrix}. \tag{23}$$

The algebraic representation of rotation is useful here since, though the inclination estimates (17), (18) and (20) are computed in different ways, any one of them may be written as

$$\hat{\theta}_i = \theta_i + b_\theta + \mu_\theta. \tag{24}$$

Here b_θ contains mostly low-frequency perturbations, such as accelerometers' bias values, μ_θ contains mostly high-frequency perturbations, such as components' thermal noise, and θ_i is the true position of the i^{th} link.

B. Mechanical three-link planar arm

Our three-link planar arm rig is show in Fig. 4. The first two joints are actuated with 70 W graphite brush DC-motors including two dedicated digital EPOS 24/5 motion controllers. Coupled with planetary gearheads, the motor-gear assembly produces output torque of about 20 Nm, transmitted via stiff toothed belts to the first two joints of the arm. The third joint can be moved freely. Due to mechanical constraints, a SICK DGS66 hollow-shaft encoder [16], 10 000 pulses per revolution, was mounted on the 1st joint and fixed to the base platform of the arm. Heidenhain ROD 486 encoders [17], 5000 sine waves per revolution, with IVB 102 interpolation units for 100-fold resolution enhancement were mounted on the 2nd and 3rd joints' axles. A PowerPC-based dSpace DS1103 system [18] was used for the motor control and state estimation at a rate of 500 Hz. A single motion reconstruction cycle took some 5-6 % of the 0.002 s sample time. Interface to the rig's motion controllers and sensory data was through the CAN-bus operating at 1 Mbit/s.

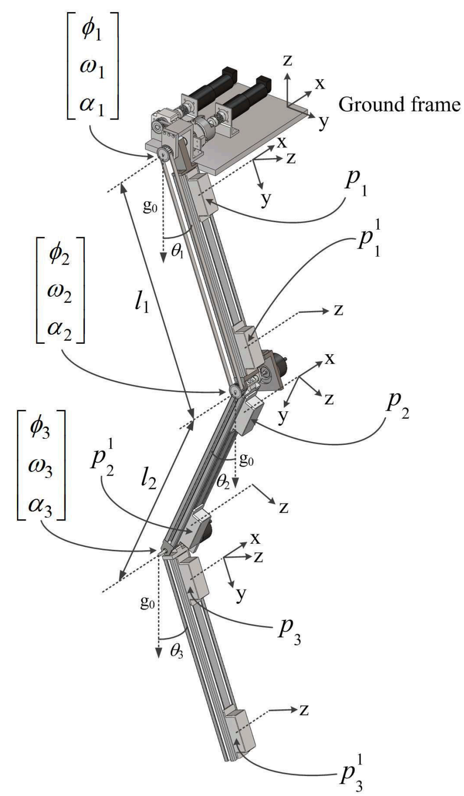

Fig. 4. Mechanical three-link planar arm comparable to a rigid multi-body assembly, $l_1 = l_2 = 0.47$ m. The combined x-axis rate gyro and triaxial accelerometer MEMS components [10] are located at $p_1 = [0\ 0.14\ 0.03]^T$ m, $p_1^1 = [0\ 0.44\ 0.03]^T$ m, $p_2 = [0\ 0.10\ 0.03]^T$ m, $p_2^1 = [0\ 0.45\ 0.03]^T$ m, $p_3 = [0\ 0.13\ 0.03]^T$ m, and $p_3^1 = [0\ 0.45\ 0.03]^T$ m. Since the motion permitted is vertically planar, the accelerometers at points p_i^2 in Fig. 3 for direct angular acceleration sensing can be omitted.

C. Angular resolutions

Table I provides a comparison of sensor resolutions according to the manufacturers' data sheets, including the traditional position differentials at 500 Hz. As the DS1103 provides for an additional 4-fold pulse subdivision, the arm's position reference from the high-accuracy encoders, which require mechanical contact to the joint axles, has a final resolution substantially higher than what is reported in the prior work cited. The MEMS rate gyros located at p_1, p_2, and p_3 utilized 1.15 %, 0.70 %, and 0.85 % x-axis calibration scale factors in (1), respectively. The identified scale factors represent experimental averages, for which the rig was used as a rate table for an encoder-differentiated angular velocity reference. Similarly, calibration look-up tables were implemented by simple arrays for the MEMS accelerometers' runtime bias compensation using a 3 deg step size with linear interpolation. In other words, the rig was also used as a turn table to cover the inclination bias that could not be expressed as a pure rotation; i.e., by determining the scale factor matrix and the bias values of the model (3).

TABLE I

JOINT SENSOR RESOLUTIONS AT 500 HZ.

Kinematic quantity	SCC1300-D02	DGS66	ROD 486
Position (deg)	$0.032^\dagger$	0.009	0.00018
Angular velocity (deg/s)	$0.02^\ddagger$	4.5	0.09
Angular acceleration (deg/s^2)	10	2250	45

† the accelerometer has a resolution of 0.56 mg per least significant bit.

‡ the gyro has a resolution of 0.02 deg/s per least significant bit.

D. Real-time joint position estimation

Under the assumption that the links of the assembly behave as rigid bodies, estimates of the joint positions can be given by

$$\hat{\phi}_i = \hat{\theta}_i - \hat{\theta}_{i-1},\ i = 1, 2, 3 \tag{25}$$

where the "ground" frame's rotation around x-axis is simply included by using the horizontal position as our reference, i.e. $\hat{\theta}_0 = 0$ deg. Fig. 5 plots the joint position errors for which the "true" joint positions ϕ_i were obtained from the encoders:

$$\Delta\phi_i = \phi_i - \hat{\phi}_i,\ i = 1, 2, 3. \tag{26}$$

The large errors of the standard estimate (17) are proportional to the distance between the used MEMS accelerometers at p_1, p_2, and p_3 and the motion-generating rotation axles. The motion compensated generalization (18) is, conversely, dominated by zero-centered high frequency perturbations. Thus, the both estimates are clearly useless for any kind of differentiation of motion derivatives. However, the complementary filtered positions based on (20) remain within ± 1 deg errors and are, in principle, only susceptible to inclination-dependent accelerometer bias values and motion-dependent scale factor nonlinearities, both of low-frequency content. The stochasticity of composite input-output nonlinearities, such as the total sensitivity and hysteresis rated for (1) and (3) by the MEMS manufacturer, plays a role at high 60-100 deg/s rates. Table II summarizes the results and, if the configurations in Figs. 2 and 3 are compared with each other, the added accelerometers for direct angular acceleration sensing add position nonlinearities marginally.

E. Angular velocity and acceleration estimates

We will next compare the estimates (7), (8) and (9) with an optimal zero-bias differentiation designed for real-time control. An optimal estimate of the 1st derivative of joint position (25) with respect to time t can be given by

$$\omega_i(t) \approx \sum_{j=0}^{m-1} \frac{A(j)\hat{\phi}_i(t - jT_s)}{T_s} \tag{27}$$

and, similarly, an optimal estimate of the 2nd derivative can be given as

$$\alpha_i(t) \approx \sum_{j=0}^{m-1} \frac{B(j)\hat{\omega}_i(t - jT_s)}{T_s} \approx \sum_{j=0}^{m-1} \frac{C(j)\hat{\phi}_i(t - jT_s)}{T_s^2} \tag{28}$$

for which the coefficients A, B and C are found in [14]. The best performing ones are also given here. Note also that any low-frequency bias in (9) can be removed without unwanted delay by the following complementary I-type control design

$$\hat{\alpha}_i^{\mathrm{I}} = \hat{\alpha}_i + \hat{b}_\alpha, \hat{\dot{b}}_\alpha = k_{\mathrm{I}}(\hat{\dot{\omega}}_i - \hat{\alpha}_i^{\mathrm{I}}), \tag{29}$$

since the gyro-based estimate (8) is bias-free but plagued by high-frequency perturbations due to the differentiation. Because errors arise with the encoder references at high sampling rates from noise or quantization effects of derivatives, Tables III and IV present results at standstill. The complementary filtered high-bandwidth positions based on (20) were differentiated in the above optimum manner for a comparison. The reported lags are indicative but, if the tabulated 1 ms delay of our MEMS electronic's cycle time is excluded, the directly sensed MEMS motion derivatives (7) and (9) are lag-free. If a further reference is made with the optimum derivatives in Table IV, results of the direct angular acceleration sensing (9) are clearly the best and in excellent agreement with the primary theoretical finding (13), particularly, if recalling the limited dimensions of the rig. For a visual comparison, a set of three estimates of the arm's 3rd joint's angular acceleration are shown in Fig. 6.

IV. DISCUSSION AND CONCLUSION

The novel multi-MEMS configuration, which is illustrated in Fig. 3, facilitates direct angular acceleration measurement by capturing the rig's full state of motion. Motivated by the fact that a low-cost angular acceleration sensor with good resolution at low angular rates is not available at present, it requires three linear accelerometers with low cross-axis sensitivity more than the minimum general case configuration shown in Fig. 2. If considering our target application field of heavy-duty hydraulic manipulators, where the underlying geometrical rigid multi-body model is most often satisfied, our primary theoretical finding (13) is broadly applicable and without any hint of instability.

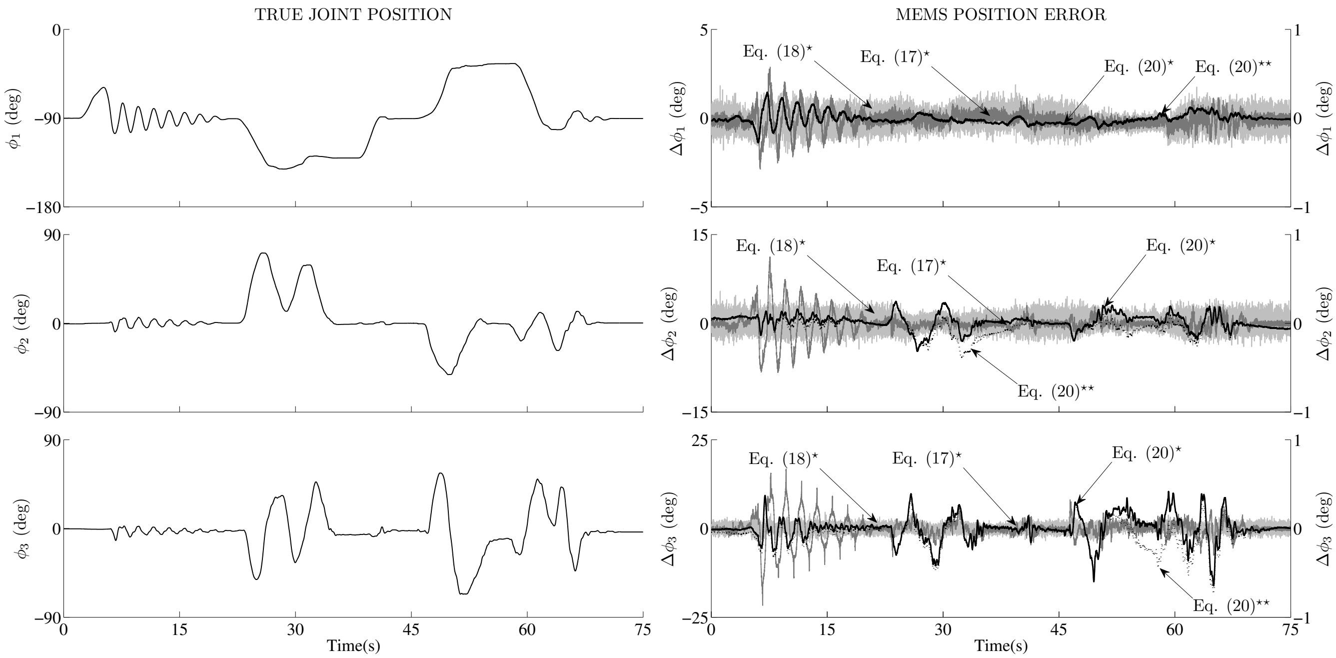

Fig. 5. A comparison of the different joint position sensing methods using the high-accuracy encoder benchmarks. Note the scales of the error graphs: the standard inclination estimate (17) as well as its motion compensated equivalent (18) use the y-axis on the left and the two PI-type complementary filters (20) use the y-axis on the right. The superscripts * and ** distinguish between the MEMS configurations illustrated in Fig. 2 and Fig. 3, respectively. Sensitivity residues of high rates from ± 60 to ± 100 deg/s reach notable levels as shown in the complementary filtered positions; see also Table II.

TABLE II

SUMMARY OF JOINT POSITION (25) SENSING ERRORS USING ENCODER BENCHMARKS AT 500 HZ SAMPLING RATE.

	Eq. (17)*			Eq. (18)*			Eq. (20)*			Eq. (20)**		
	Joint 1	Joint 2	Joint 3	Joint 1	Joint 2	Joint 3	Joint 1	Joint 2	Joint 3	Joint 1	Joint 2	Joint 3
PAE† (deg)	2.89	11.19	21.69	2.00	7.23	10.93	0.29	0.32	0.65	0.29	0.39	0.74
RMSE‡ (deg)	0.49	1.77	3.04	0.46	1.47	1.76	0.06	0.09	0.14	0.06	0.10	0.16

†Peak absolute error, ‡Root mean square error, *Configuration in Fig. 2, **Configuration in Fig. 3

TABLE III

STANDSTILL JOINT ANGULAR VELOCITY ERRORS AT 500 HZ SAMPLING RATE.

	Eq. (7)			Eqs. (20)** & (25) & (27)		
	Joint 1	Joint 2	Joint 3	Joint 1	Joint 2	Joint 3
RMSE (deg/s)	0.068	0.081	0.078	0.062	0.072	0.073
Lag (ms)	1			5-6		

Optimal finite difference filter (27) coefficients $A = [5\ 3\ 1\ \ -1\ \ -3\ \ -5]/35$.

TABLE IV

STANDSTILL JOINT ANGULAR ACCELERATION ERRORS AT 500 HZ SAMPLING RATE.

	Eq. (8)			Eqs. (7) & (28)			Eqs. (20)** & (25) & (28)			Eq. (9)		
	Joint 1	Joint 2	Joint 3	Joint 1	Joint 2	Joint 3	Joint 1	Joint 2	Joint 3	Joint 1	Joint 2	Joint 3
RMSE (deg/s^2)	31.38	35.74	33.50	8.64	10.25	9.86	13.57	15.78	16.05	6.78	8.74	8.38
Lag (ms)	2-3			5-6			5-6			1		

Optimal finite difference filter (28) coefficients: $B = [5\ 3\ 1\ \ -1\ \ -3\ \ -5]/35$ and $C = [5\ \ -1\ \ -4\ \ -4\ \ -1\ 5]/28$.

1 ms of all the delays is due to our MEMS electronic's cycle time.

The gyro-aided joint position sensing was discussed as an easily obtainable high-bandwidth quantity, and just to verify the full motion state estimation effectiveness of the presented multi-MEMS configuration over the axle-wise contact-type angular sensors such as encoders. As detailed in Table II, achieving the worst-case joint position error less than ± 1 deg in relatively fast motion without the usual delay using solely MEMS rate gyros and linear accelerometers is a good result on its own, too. The related PI-type complementary filter keeps assumptions to a minimum and is completely general in the sense that any 3-DOF rotation can be represented by three 1-DOF rotations. To sum up, the typical similarity of a 3-DOF filter architecture (see e.g. [13]) to that of (19) makes the inclination sensing by (15) widely applicable.

Because of the relatively effortless "strap-down" installation, immunity against local magnetic disturbances, size

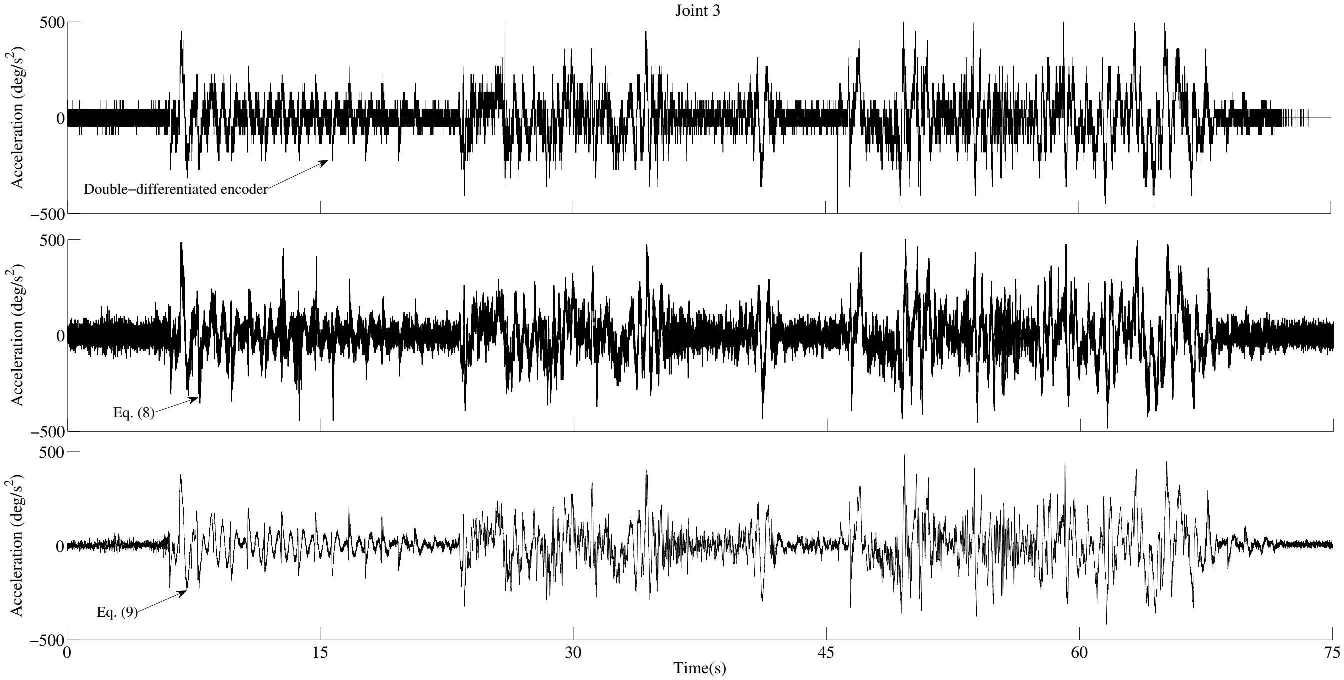

Fig. 6. A plot illustrating the double-differentiated encoder (Table I), indirectly differentiated MEMS rate gyro (8), and MEMS accelerometer-based direct sensing (9) of angular acceleration. Whereas the encoder benchmark has a low noise density only at a perfect standstill, resolution of the proposed direct angular acceleration sensing (9) remains fine at low rates throughout the experiment, see also Table IV.

and cost advantage over the contact-type angular sensors, the geometry-aided MEMS motion sensing is currently experimented on a heavy-duty HIAB 031 manipulator for inverse kinematics and active damping control. Since the proposed multi-MEMS mounting is favored by the HIAB 031 manipulator's large dimensions, the angular acceleration readings (9) contain some 30–40 % less random variation than that reported in Table IV or what is correspondinly observable in Fig. 6. This is a clear advantage from the low-cost motion control perspective, see [19] for further discussion.

Acknowledgment

The authors are very grateful to researchers Erkki Lehto and Janne Koivumäki for their superb support with the MEMS electronics as well as the mechanical rig design.

References

[1] S. J. Ovaska and S. Väliviita, "Angular acceleration measurement: A review," *IEEE Trans. Instrum. Meas.*, vol. 47, no. 5, pp. 1211–1217, Oct. 1998.

[2] M. Bertoluzzo, G. S. Buja, and E. Stampacchia, "Performance analysis of a high-bandwidth torque disturbance compensator," *IEEE/ASME Trans. Mechatronics*, vol. 9, no. 4, pp. 653–660, Dec. 2004.

[3] J. Vihonen, J. Honkakorpi, J. Mattila, and A. Visa, "Geometry-aided MEMS motion state estimation for multi-body manipulators," in *IEEE/ASME Int. Conf. on Advanced Intelligent Mechatronics (AIM)*, Wollongong, Australia, July 2013, pp. 341–347.

[4] M. J. Caruso, "Applications of magnetic sensors for low cost compass systems," in *IEEE Pos. Loc. and Nav. Symp.*, Aug. 2000, pp. 177–184.

[5] J. Leavitt, A. Sideris, and J. Bobrow, "High bandwidth tilt measurement using low-cost sensors," *IEEE/ASME Trans. Mechatronics*, vol. 11, no. 3, pp. 320–327, June 2006.

[6] F. Ghassemi, S. Tafazoli, P.D. Lawrence, and K. Hashtrudi-Zaad, "Design and calibration of an integration-free accelerometer-based joint-angle sensor," *IEEE Trans. Instrum. Meas.*, vol. 57, no. 1, pp. 150 – 159, Jan. 2008.

[7] H. Dejnabadi, B. M. Jolles, and K. Aminian, "A new approach to accurate measurement of uniaxial joint angles based on a combination of accelerometers and gyroscopes," *IEEE Trans. Biomed. Eng.*, vol. 52, no. 8, pp. 1478–1484, Aug. 2005.

[8] P. Cheng and B. Oelmann, "Joint-angle measurement using accelerometers and gyroscopes - a survey," *IEEE Trans. Instrum. Meas.*, vol. 59, no. 2, pp. 404–414, Feb. 2010.

[9] A. J. Padgaonkar, K. W. Krieger, and A. I. King, "Measurement of angular acceleration of a rigid body using linear accelerometers," *Trans. ASME*, vol. 42, no. 3, pp. 552–556, Sept. 1975.

[10] Murata Electronics Oy, "SCC1300-D02 combined x-axis gyroscope and 3-axis accelerometer with digital SPI interfaces," www.muratamems.fi, Aug. 2012.

[11] R. G. Brown and P. Y. C. Hwang, *Introduction to random signals and applied Kalman filtering*, Wiley, New York, NY, 1997.

[12] D. H. Titterton and J. L. Weston, *Strapdown Inertial Navigation Technology*, Institution of Engineering and Technology, 2004.

[13] R. Mahony, T. Hamel, and J-M. Pflimlin, "Nonlinear complementary filters on the special orthogonal group," *IEEE Trans. Autom. Control*, vol. 53, no. 5, pp. 1203–1218, June 2008.

[14] A. J. L. Harrison and D. P. Stoten, "Generalized finite difference methods for optimal estimation of derivatives in real-time control problems," *Proc. Instn. Mech. Engrs.*, vol. 209, no. 2, pp. 67–78, May 1995.

[15] W. T. Higgins, "A comparison of complementary and Kalman filtering," *IEEE Trans. Aerosp. Electron. Syst.*, vol. 11, no. 3, pp. 321–325, May 1975.

[16] SICK AG, "DGS60, DGS65 and DGS66: Incremental encoders for rough environmental conditions," www.mysick.com, Sept. 2006.

[17] Heidenhain, "Rotatory encoders," www.heidenhain.de, Nov. 2011.

[18] dSpace GmbH, *DS1103 PPC Controller Board Features*, Mar. 2005, Release 4.2.

[19] J. Honkakorpi, J. Vihonen, and J. Mattila, "MEMS-based state feedback control of multi-body hydraulic manipulator," in *IEEE/RSJ Int. Conf. on Intelligent Robots and Systems (IROS)*, Tokyo, Japan, Nov. 2013, accepted for publication.